Mechanisms of mass transport during coalescence-induced microfluidic drop dilution

William S. Wang and Siva A. Vanapalli*
Department of Chemical Engineering, Texas Tech University, Lubbock, Texas 79409, USA
(Received 1 May 2016; published xxxxxx)

Confinement-guided coalescence of drops in microfluidic devices is an effective means to manipulate the composition of individual droplets. Recently, Sun *et al.* [Lab Chip **11**, 3949 (2011)] have shown that coalescence between a long moving plug and an array of parked droplets in a microfluidic network can be used to flexibly manipulate the composition of the static droplet arrays. However, the transport mechanisms underlying this complex dilution process have not been elucidated. In this study, we develop phenomenological models and perform particle-based numerical simulations to identify the key mass transfer mechanisms influencing the concentration profiles of drops during coalescence-induced drop dilution. Motivated by experimental observations, in the simulations we consider (i) advection within the moving plug, (ii) diffusion in the moving plug and parked droplets, (iii) fluid advection due to initiation of coalescence, and (iv) advection in the coalesced plug due to the continuous phase flowing through the gutters in noncircular microchannels. We find that the dilution process is dominated by diffusion, recirculation in the moving plug, and gutter-flow-induced advection, but is only weakly affected by coalescence-induced advection. We show that the control parameters regulating dilution can be divided into those influencing the duration of mass transfer (e.g., plug length and velocity) and those affecting the rate of mass transfer (e.g., diffusion and gutter-flow-induced advection). Finally, we demonstrate that our simulations are able to predict droplet concentration profiles in experiments. The results from this study will allow better design of drop dilution microfluidic devices. Furthermore, the identification of gutter-flow-induced advection as an alternative mass transfer mechanism in two-phase flows could potentially lead to more efficient means of oil recovery from droplets trapped in porous media.

DOI: 10.1103/PhysRevFluids.00.004000

I. INTRODUCTION

Droplet-based microfluidics involves the production and manipulation of monodisperse droplets where each droplet acts as a distinct microreactor [1]. Driven by benefits such as sample digitization, reduced reagent consumption, high-throughput analysis, and sensitive detection, droplet-based microfluidics has found numerous applications in biochemical analysis, cell-based assays, and material synthesis [2–5]. Paralleling the needs of applications, fundamental advances have also been made in understanding and controlling the generation, breakup, coalescence, and trafficking of microfluidic droplets [6–9].

A central requirement for several droplet-based applications [1,4,10,11] is the ability to flexibly change the reagent concentration in microfluidic drops across a wide range—a process that is analogous to serial dilution of reagents at the macroscale. To achieve dilution, one class of methods employs strategies to vary the local composition of the fluid mixture prior to droplet generation, producing one-dimensional (1D) trains of moving drops with distinct concentrations [1,10–19]. Another class of methods involves inducing coalescence repetitively between the generated droplets, either passively or actively [20–29].

*siva.vanapalli@ttu.edu

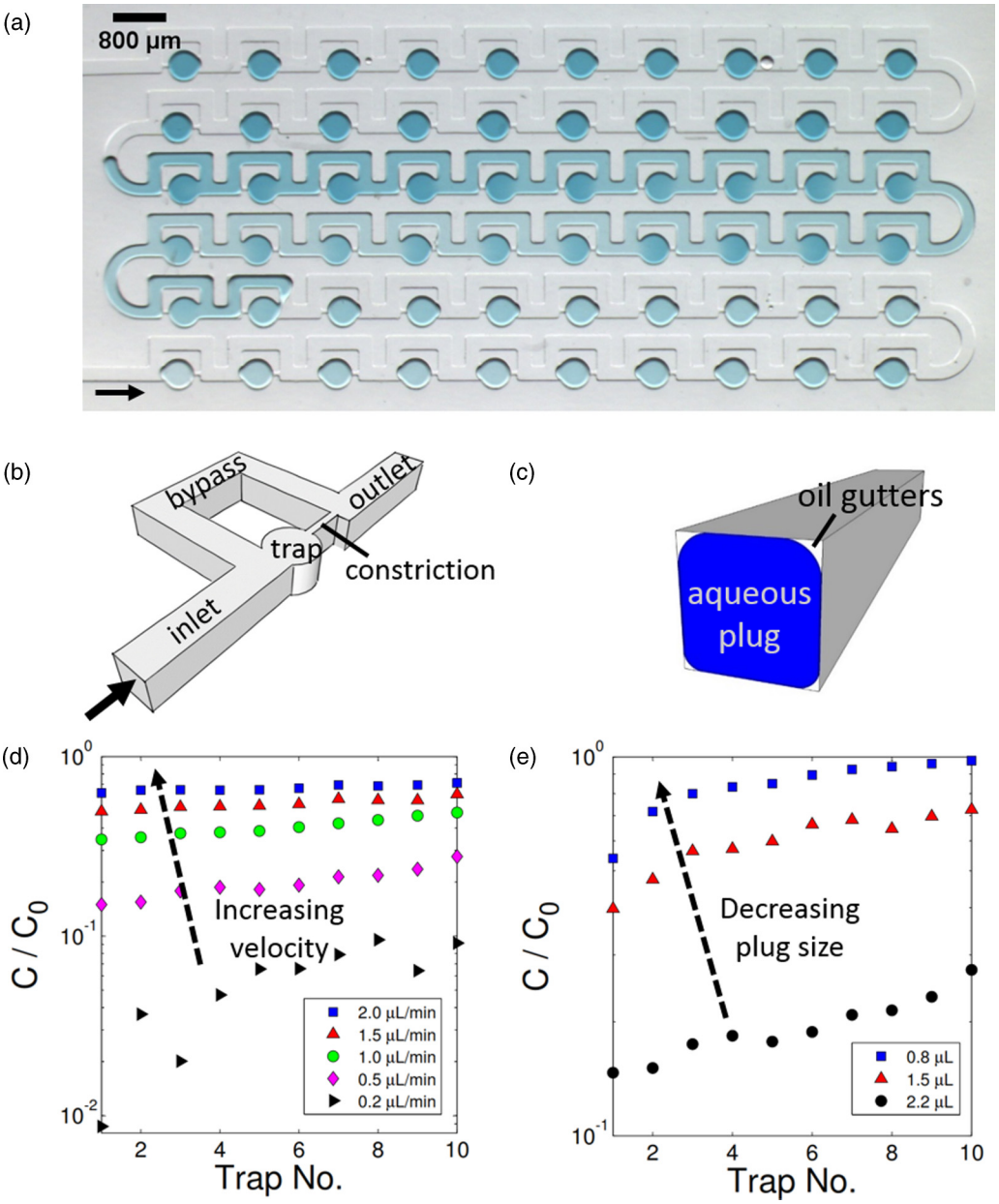

FIG. 1. Dilution of SDAs with moving plugs: (a) a 2.2-μl water plug in mineral oil traveling bottom to top through a 60-trap SDA in which each static drop initially contains the same amount of aqueous dye, C_0; (b) 3D schematic of a recurring trapping loop in an SDA; (c) cross-sectional schematic of a microfluidic channel in an SDA illustrating the presence of gutter flows around an aqueous plug; (d) and (e) concentration profiles for the first ten traps (450-μm diameter) for various flow rates (0.2–2.0 μl/min) and plug sizes (0.8–2.2 μL), respectively, using device in (a) with 200 $\times$ 200-μm cross-section channels; data from Sun *et al.* [25].

Recently, we showed that coalescing long plugs with an array of drops immobilized in a microfluidic parking network (MPN) can be used to achieve dilution (see Fig. 1) [19,25]. The MPN network contains a series of parking loops with each loop containing a trap chamber and a

bypass channel. The dilution method involves injecting two long plugs sequentially into the MPN network. As the first plug moves through the MPN, it fills the traps. When the tail of this plug reaches the entrance of each parking loop, it sequentially ruptures, creating a static droplet array (SDA), where each droplet has the same concentration. The dilution occurs when the second plug coalesces with each of the droplets, enabling mass transfer between the traps and the plug. Because the concentration of solute in the moving plug varies with position along the plug, the flux in and out of each trap varies, and different concentration gradations are generated across the SDA.

This method is flexible, as the reagent concentration from drop to drop can be manipulated in fine gradations either by varying the flow rate or the volume of the diluting plug, as shown in Figs. 1(d) and 1(e), respectively. In contrast to methods that create concentration gradations in 1D droplet trains [1,10–19], this dilution approach offers distinct advantages: (i) Identification and imaging of these two-dimensional (2D) static droplet arrays (SDAs) is easier because the drops are located at prescribed coordinates; and (ii) SDAs can be studied for long periods of time, whereas 1D moving droplet trains are limited by droplet residence time, making SDAs particularly suitable for reactions with slow kinetics.

Despite the flexibility and benefits of this microfluidic drop dilution approach, a deeper understanding of the mechanisms controlling mass transfer between confined coalesced droplets of differing composition is lacking. Previous studies of coalescence have been pursued in configurations that are different from dilution-motivated geometries, such as coalescence of unconfined droplets [30–32] or only slightly confined droplets [33]. In our system, we have a moving diluting plug and static droplets, and these two coalescing bodies merge but do not significantly alter the rest of their shapes except for the interface. Moreover, the gutters in the corners of the rectangular channel cross sections [see Fig. 1(c)]—which are typical of most microfluidic geometries and have been shown to be important in droplet production at a T junction [34,35], droplet trapping [21,26], and dilution of droplets [20]—enable the continuous oil phase to flow and "stir" the fluid inside. As a result, the process of mass transfer is rather complex, and none of the microfluidic studies focusing on droplet dilution [1,10–29] have pursued modeling to describe the evolution of concentration during coalescence-induced dilution.

In our system, mass transfer is expected due to several phenomena: (i) the initial coalescence event triggered by the rupture of the thin film of continuous phase, (ii) advection due to flow patterns that are established while the diluting plug is coalesced with the static droplets, and (iii) mass diffusion within the coalesced plug that results from local concentration variations. It is unclear to what extent each of these mechanisms influences the final concentrations in the SDA, and how system parameters influence the final dilution profile. For example, in the plot of concentration versus trap number in Fig. 1(d), a tenfold increase in plug velocity unexpectedly causes nearly two orders-of-magnitude increase in final concentration for the first trap. Such nonlinear effects must be understood in order to accurately predict and control the concentration profiles generated using coalescence-induced drop dilution.

In this study, we pursue particle-based simulations to provide insights into the mechanisms regulating mass transport during coalescence between a moving plug and a stationary drop(s). In Sec. II, we formulate the problem by considering a simplified microfluidic geometry. In Sec. III, we first start with a basic model that includes only the most obvious elements—advection in the plug and diffusion throughout all aqueous phases. Next, we refine the phenomenological model by including further elements—such as delayed coalescence, coalescence-induced advection (CIA), and gutter-flow-induced advection (GFIA)—to see how they affect mass transfer. Our simulation algorithm is presented in Sec. IV. Finally, in Sec. V, we demonstrate how simulations based on our phenomenological model reflect the same qualitative trends that are observed in experiments, such as how concentration profiles are affected by changes in plug volume, plug velocity, and changes in network geometry. In this section, we also assess the importance of the different transport mechanisms. Our results show that GFIA contributes significantly to mass transport during confinement-guided coalescence, highlighting its importance for microfluidic drop dilution.

II. PROBLEM FORMULATION

The basic approach underlying the dilution of SDAs is coalescence between a moving plug and an array of stationary drops. We seek to model the underlying mass transfer processes phenomenologically. Although the diluting plug in the actual SDA shown in Fig. 1(a) moves through a circuitous path and coalesces with circular traps, our model uses a simplified geometry and considers only the most basic elements, such as plug volume (and length), trap volume (and therefore static droplet volume), and trap spacing (according to linearized path length between traps), and plug-trap interface size. These simplifications reduce the initial number of variables in our system and make it easier to identify relationships between the model parameters and predicted results.

As shown in Fig. 2(a), our simplified geometry involves a moving 2D rectangular plug that contacts trapped drops modeled as stationary square fluid elements. Because the computation time could be minimized by restricting the type of boundaries to linear segments and by minimizing the number of boundaries, we chose to approximate the circular traps with square-shaped traps. For example, the 450-μm-diameter circular trap is modeled as a 400 $\times$ 400-μm square trap, resulting in cross-sectional areas that deviate less than 1% from each other. Since the trap fluid in our model is either entirely or mostly stationary [except for a perimeter flow when simulating gutter-flow-induced advection as shown in Fig. 2(c)], the use of an equal-area trap—such as a square—should yield nearly identical diffusional mass transfer in our 2D simulations.

System characteristics

Given that we have simplified the SDA geometry, here we discuss the important dimensionless numbers and relevant time scales based on experimental data. The experiments [25] inspiring the phenomenological model and simulation parameters were performed in square microfluidic channels of approximately 200 $\times$ 200 μm (cross-sectional area $A = 4 \times 10^4\ \mu\text{m}^2$) and using volumetric flow rates, Q = 12–120 μl/h, corresponding to plug velocities, $U_p \approx$ 80–800 μm/s. Reynolds numbers, $\text{Re} = \frac{\rho_{aq} \text{W} U_p}{\mu_{aq}} \approx 1.7 \times 10^{-2}$ to 0.17, where the aqueous-phase density, $\rho_{aq} = 998\ \text{kg/m}^3$, the channel width, $W = 200\ \mu$m, and the aqueous-phase viscosity, $\mu_{aq} = 0.001$ Pa s. While inertial forces are relatively weak compared to viscous forces, they are not negligible in this range. The capillary number $\text{Ca} = \frac{\mu_{\text{oil}} U_p}{\gamma} \approx 5 \times 10^{-5}$ to 5×10^{-4}, where the viscosity of the oil outer phase $\mu_{\text{oil}} =$ 0.030 Pa s, and the interfacial tension, $\gamma \approx 0.050$ N/m. The Péclet number, $\text{Pe} = \frac{U_p W}{D} \approx$ 30–300, where $D(=500\ \mu\text{m}^2/\text{s}$ [36,37]) is the diffusivity of the fluorescein molecule. Note that in our simulations, we assume that for long plugs, the plug velocity (U_p) is of the same order of magnitude as the mean continuous-phase fluid velocity (U) [6,38].

Note that Pe > 1 might imply that the contribution of diffusion is negligible compared to advection. However, a consideration of two specific time scales establishes the importance of diffusion: diffusion time across the channel width (t_D), and contact time (t_C), which is the length of time the moving plug is coalesced with a given trapped droplet. The diffusion time across the channel width is given by $t_D = \frac{\text{W}^2}{2D} \approx 40$ s. Contact time can be determined from the plug length (L_p) and plug velocity (U_p) as $t_C = \frac{L_p}{U_p}$. In the experiments, plug volumes (V_p) ranged from 0.8 to 4 μl [19,25], corresponding to plug lengths of 20–100 mm. Using a typical plug length of 25 mm and a velocity of 500 μm/s, contact time is 50 s. Because contact time and diffusion time are of the same order of magnitude, this means there is sufficient time for the fluorescein tracer to diffuse out from the trap and across the entire width of the plug before the plug detaches from the trapped droplet. The effects of diffusion therefore cannot be ignored, and both diffusion and advection should be considered in the phenomenological model.

III. EXPERIMENTAL EVIDENCE AND MODELING OF MASS TRANSPORT MECHANISMS

Our approach in building a phenomenological model for the dilution of SDAs with moving plugs involves identifying transport mechanisms (see Fig. 2) based on actual experimental observations,

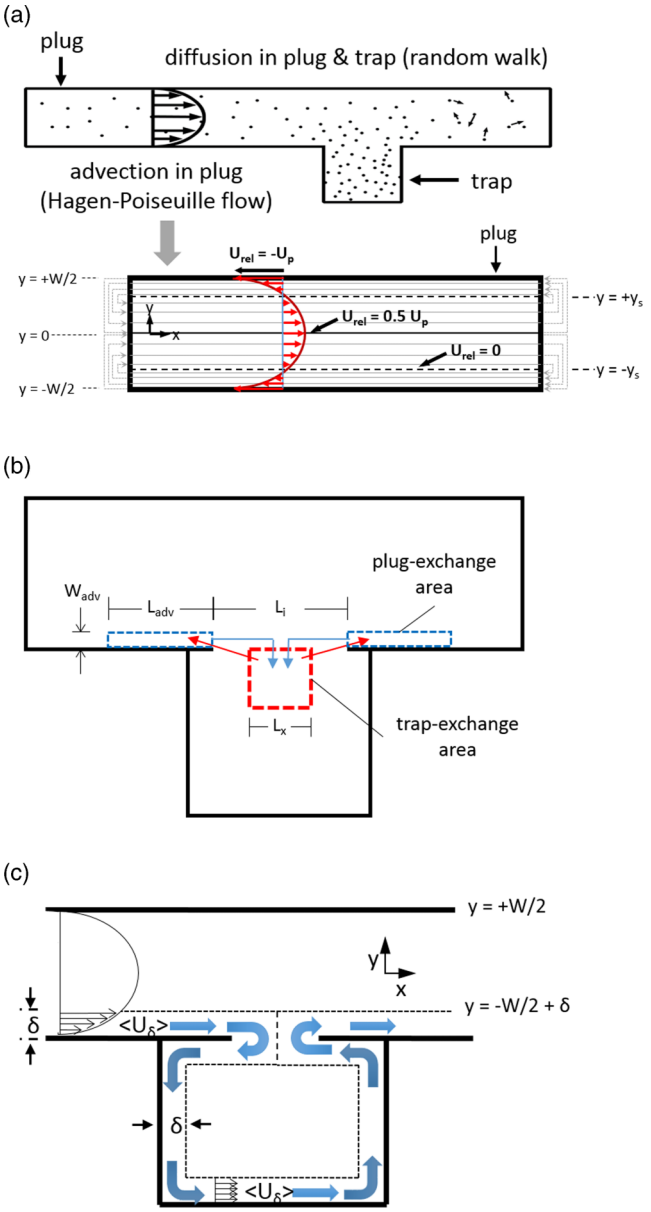

FIG. 2. Models for mass transport mechanisms used in simulations: plug advection, diffusion, coalescence-induced advection (CIA), and gutter-flow-induced advection (GFIA). (a) The basic model involves advection within the moving plug with recirculation at the ends of the plug, and diffusion throughout the moving plug and the trapped drop. The advection in the plug is modeled using the Hagen-Poiseuille flow with recirculation at the ends (from the perspective of moving plug) and diffusion is modeled using random walk. Relative velocity profile is shown in red; recirculating streamlines shown in light gray. (b) A model for CIA. Upon coalescence, particles within a trap-exchange area are exchanged with any particles in two equally sized plug-exchange areas to simulate CIA. Relevant parameters include plug-trap interface length (L_i), length of square trap-exchange area (L_x), and length and width of the advected plug-exchange areas ($W_{\rm adv}$ and $L_{\rm adv}$, respectively). (c) A model for GFIA. A 2D schematic of trap area showing the near-wall layer of thickness δ redirected from the plug along the perimeter of the trap, shown by blue arrows. Particles in this fluid layer move at the same velocity $\langle U_\delta \rangle$ along the perimeter of the trap.

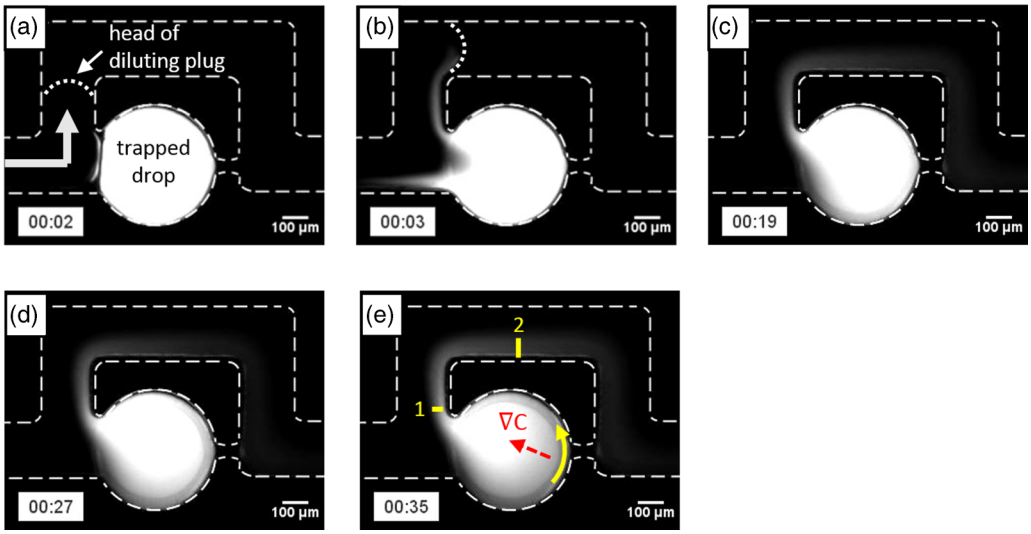

FIG. 3. Time-lapse experimental images (a)–(e) of a moving plug of pure water driven by an outer mineral oil phase and diluting a trapped fluorescein-dyed aqueous droplet. The head of the diluting plug is present only in (a), (b) and it has moved out of the field of view in (c)–(e). In (e), the widths 1 and 2 (∼50 and ∼100 μm, respectively) indicate the width of the stream of dye particles being carried downstream. The red dashed arrow in the trap region designates a concentration gradient from the wall towards the center, and the yellow solid curved arrow designates a counterclockwise concentration gradient along the trap perimeter, indicating a counterclockwise evacuation of fluorescein.

developing simple models for each of the transport mechanisms and then implementing them in particle-based simulations to assess the relative importance of each transport mechanism with respect to final concentrations. First, we begin with a basic model [Fig. 2(a)] that includes only the most obvious transport mechanisms—such as advection in the plug and diffusion throughout all aqueous phases. Next, we introduce additional elements into the mass transfer model—such as delayed coalescence, coalescence-induced advection [CIA; see Fig. 2(b)], and gutter-flow-induced advection [GFIA; see Fig. 2(c)]—to see how well they bridge the gap between simulation and experiment. This bottom-up modeling approach where the complexity is hierarchically introduced enables us to identify the relative importance and effect of each transport mechanism on the inherently complex nature of mass transfer in our drop dilution system.

A. Advection in the moving plug

In experiments, advection within the moving plug clearly plays an important role in mass transfer. In the time-lapse experimental images shown in Fig. 3 (for original video, see Electronic Supplementary Information, or "ESI", Sec. 4, Movie S3 of Sun *et al.* [25]), as the moving plug travels downstream, the plug visibly carries dye particles that have exited the trap downstream as the plug progresses through the network. The importance of advection is also corroborated by the fact that Pe>1, as discussed in Sec. II A. We therefore include the advection of particles due to the fluid motion in the moving plug.

We model the flow in the moving diluting plug using a parallel plate approximation proposed by Handique and Burns [39]. The fluid within an immiscible liquid plug moving through a narrow gap between two parallel plates follows recirculating paths around two vortices, with the vortices isolated in two halves [39], as shown in Fig. 2(a) (bottom). A plane between and parallel to the two plates divides the plug into halves. The combination of pressure-driven Hagen-Poiseuille flow and

closed boundaries requires a parabolic velocity profile in the body of the plug and recirculation at the front and rear of the plug, as shown in Fig. 2(a).

From the frame of reference of the moving plug, the relative velocity profile is given by Eq. (1), where U_p is the magnitude of the plug velocity (which one could measure by tracking the position of either the head or tail over time from a fixed frame of reference) [39].

$$U_{\text{rel}} = 0.5\, U_p \left[1 - 3\left(\frac{y}{W/2}\right)^2\right]. \tag{1}$$

Note how the fastest advancing (or forward) relative velocity is in the center of the plug ($y = 0$) and has a magnitude of $0.5\, U_p$. The fastest receding (or rearward) relative velocity is $-U_p$ at the walls, which satisfies a no-slip condition at the boundaries. In both halves of the plug, there is a stagnation line ($y = \pm y_s$) at about 0.577 times the half-channel width from the centerline where the relative velocities are zero, which means any liquid in that region would simply travel at the same speed as the plug and would not appear to advance or recede relative to the plug. Using particle image velocimetry (PIV), several groups have confirmed that fluid does in fact circulate in elongate vortices in each half of the plug [40–43].

Recirculation of particles between advancing and receding sections within each vortex is accomplished by performing a volumetric flow rate balance—essentially a mass balance—around the stagnation line and is explained in Appendix A of the ESI [39]. For example, to identify the corresponding receding y coordinate for an advancing particle that is to be recirculated upon reaching the front of the plug, we simply identify the receding y coordinate which satisfies the following volumetric flow rate balance: flow rate between the stagnation line and the advancing y coordinate = flow rate between the stagnation line and the receding y coordinate. The advancing and receding volumetric flow rates between the moving particle and the stagnation line must be identical, otherwise there would be a nonphysical accumulation or loss of mass at the end caps.

B. Diffusion

As suggested by the comparison of diffusion time across the channel width and contact time in Sec. II A, diffusion is also important for mass transfer during drop dilution. In Fig. 3(e), for example, the narrow stream of particles leaving the trap region has a width that roughly doubles from about 50 to about 100 μm after traveling $\approx$1000 μm downstream. This indicates that the dye is indeed diffusing across the width of the channel over time. In the trap, the left-pointing arrow indicates the presence of a concentration gradient across the confined droplet. Assuming the velocities are substantially lower in the trap region than in the main channel and bypass channel, the presence of concentration gradients in the trap—particularly in the center, where flow is most likely to be relatively stagnant—indicates diffusion. In our phenomenological model, we therefore include the effects of diffusion throughout the moving plug and static droplets.

We model dye diffusion in the moving and static drops by imposing random displacements to the particles in the simulation. The probability distribution for a particle's displacement after a certain time (t) is Gaussian and depends on its diffusion coefficient (D) [44–46]. The standard deviation of the probability distribution for a single particle (in each independent dimension, e.g., x, y, and z)—which is the same as the root-mean-squared displacement for an ensemble of particles starting at the same location—is given by [44,47]

$$\sigma = \sqrt{\langle x \rangle^2} = \sqrt{2Dt}. \tag{2}$$

In particle-based simulations, diffusion can therefore be modeled using the random walk method [42]:

$$x_k = x_k^* + \zeta_{(x,k)}\sqrt{2D\Delta t} \quad \text{and} \quad y_k = y_k^* + \zeta_{y,k}\sqrt{2D\Delta t}, \tag{3}$$

where the new coordinates for the kth particle (x_k, y_k) are calculated by starting with the initial coordinates $(x_k^*,\ y_k^*)$ and displacing them by the product of the displacement standard deviation—which depends on D and the time step size, Δt—and a random number (ζ) that is sampled from a normal distribution with a mean of zero and a standard deviation of 1. The random numbers $\zeta_{x,k}$ and $\zeta_{y,k}$ simply denote the fact that separate random numbers are generated for the kth particle for displacements in the x and y directions.

In each simulated time step, when particles are allowed to diffuse, it is possible for particles to attempt to move beyond the plug and/or trap boundaries. When this occurs, we implement the commonly used bounce-back condition [48,49], where any particle's attempt to move beyond the system bounds is ignored for the current time step and is simply left in place. This is a reasonable alternative to the reflective-boundary condition—where particles are reflected off the boundary like a mirror—because upon reflecting off the wall, the particle still has equal probabilities of ending up either closer to or farther from the wall. Therefore leaving the particle in place (versus reflecting it) does not unnaturally skew the concentration of particles near boundaries.

C. Coalescence-induced advection

As a long plug moves through an SDA network, experimentally we often see that the head of the moving plug may enter the bypass channel and travel some distance before the body of the plug finally coalesces with the trapped droplet as shown in Figs. 3(a) and 3(b). This delayed coalescence is likely because a finite amount of time is required for the thin oil film between the plug and droplet to drain. Drainage time is a function of both normal-direction and tangential-direction approach velocities, as well as rate of deformation of the interface upon approach [50–52].

After each coalescence event in experiments, there is a sudden and violent exchange of material between the moving plug and trapped droplet: Concentrated material from the static droplets is visibly dispersed outward along the channel walls [see Fig. 3(b)]. The initial dispersion of material appears to occur much more quickly than should be possible for advection due to the standard Hagen-Poiseuille pressure-driven parabolic velocity profiles, as material near the walls appears to advance more quickly than the plug head. This suggests a phenomenon other than the standard flow profile is the driving force. Even more surprising is that concentrated material from the static droplet is also dispersed upstream of the trap against the direction of flow. Dye is dispersed several hundred micrometers upstream and downstream of the trap. Some of the plug's clear fluid can also be seen partially infiltrating the static drop. This coalescence-induced advection (CIA) could impact the final SDA concentrations. We therefore include both delayed coalescence and CIA in advanced versions of our model.

We note that CIA could be partially due to Marangoni flows [53–55] induced by gradients in interfacial tension between the moving plug and trapped droplets. Using a ring tensiometer (Krüss K100), we measured the interfacial tension between mineral oil and both pure water and aqueous solutions of food dye at the concentrations used in experiments: For pure water, $\gamma = 45.65 \pm 0.031$ mN/m; for a 20× dilution of blue food dye (Great Value, Walmart), $\gamma = 11.17 \pm 0.082$mN/m; for a 10× dilution of black food dye (Great Value, Walmart), $\gamma = 2.6$ mN/m. Since the trapped droplet contains dye [e.g., see Figs. 1(a) and 3(b)], it has a much lower interfacial tension than the moving plug of pure water [56], allowing the moving plug interface to pull material out of the trap. Based on the difference between the interfacial tensions of oil-water and oil-dye solutions, the driving force could be as high as 43 mN/m. In a prior study, Marangoni stresses caused a microdroplet of an alcohol solution to spread radially along the surface of pure water, doubling the droplet diameter in a matter of milliseconds with an interfacial tension difference or driving force of only 5.56 mN/m [55]. Moreover, another study showed that interfacial tension differences can even cause particles to migrate upstream against gravity, from a lower-elevation trough with a particle-laden fluid surface to a higher-elevation trough with pure fluid of higher interfacial tension [54]. In the study by Wen *et al.* [27], the direction of Marangoni stresses is opposite from ours with opposite results: The moving plug is dyed, and the trapped droplet is pure water. In this case, the dye is pulled from the plug into

the trap and along the inner perimeter of the trap in both directions (see Fig. 3(a) in Wen *et al.* [27]). Therefore it is likely that CIA is at least partially due to Marangoni flows.

Based on experimental observations, we know that the conversion of surface energy to kinetic energy causes an exchange of volume between the trapped droplet and the moving plug. Furthermore, the length scale of the affected area appears to be on the order of the size of the interface itself (e.g., the length): For a 200-μm-long interface, the ejected fingers upstream and downstream are a few hundred microns long, and fluid from the moving plug infiltrates the trapped droplet less than 200 μm. We therefore model CIA by a volume exchange as illustrated in Fig. 2(b).

In our 2D simulations, CIA is incorporated by defining a trap-exchange area—marked by a red square of length L_x in Fig. 2(b) within the trap region and adjacent to the plug-trap interface of length L_i— and two plug-exchange areas upstream and downstream of the plug-trap interface region—marked by blue rectangles in Fig. 2(b) with width and length of W_{adv} and L_{adv}, respectively. Consistent with experiments, the head of the moving plug is allowed to travel past the trapped droplet a user-specified distance (or "merge point" distance, Δ_{merge}) before coalescence is deemed to have occurred. Once the merge point of the simulated plug reaches the trap interface, coalescence is allowed, and the wall segment (of length L_i) at the plug-trap interface is removed to allow particle exchange between plug and trap. Any particles in the trap-exchange area are removed from the trap and distributed evenly among the two plug-exchange areas, which together occupy the same area as the trap-exchange area. Any particles in the plug-exchange areas are likewise moved to the trap-exchange area. For simulations, we predefine the size of the trap-exchange area (L_x) and the plug-exchange areas ($W_{\text{adv}} L_{\text{adv}}$)based on typical experimental observations.

D. Gutter-flow-induced advection

Generally in situations of viscous flow past an open cavity, one expects closed-streamline circulation in the cavity [57]. Moreover, circulation must be in a direction that allows velocities to match at the mouth of the cavity [57]. In this situation, we might therefore initially expect to see a clockwise fluid rotation in the experimental time-lapse images of static droplets being diluted with moving plugs in Fig. 3. However, in the experimental images of Fig. 3, we observe material being scooped in the counterclockwise direction in the trap, even though the moving plug on the left side of the trap exerts shear stresses at the trap entrance that tend to induce a clockwise circulation.

To investigate this phenomenon, we performed single-phase 2D computational fluid dynamics (CFD) simulations. As shown in Fig. 4(a), when a single-phase fluid flows through the trap geometry without a constriction, closed streamlines are observed with clockwise circulation of the fluid in the trap. This single-phase simulation result is in contradiction with our experimental observation. Moreover, the closed streamlines in this case mean that mass transfer between trap and plug can occur only through diffusion.

To proceed, we hypothesize that in a two-phase system where an outer oil phase drives an aqueous plug through an SDA with square cross-sectioned channels, there is substantial outer-phase flow in the gutter regions [see Fig. 1(c)]. Figure 4(b) is a schematic of what would likely be seen near the top and bottom of the channel: While the aqueous plug is essentially pressed against the top and bottom surfaces of the channel (except for a thin film of oil) across most of the width of the channel, there is a significant gutter region along the entire perimeter of the plug. Oil flowing in the lower part of the schematic (or the right-hand side of the moving plug) flows counterclockwise around the trap, with some of the oil exiting the trap constriction and the rest continuing counterclockwise until it leaves the trap and enters the bypass channel.

We estimate the radius of curvature of the gutters (R_{gutter}) for a stationary plug, and find that the gutter region can be substantial with $R_{\text{gutter}} \approx \text{W}/10 \approx 20\,\mu\text{m}$. We arrived at this estimate by equating the pressure differentials across the interface in the spherically shaped end caps and the cylindrically shaped gutter regions, using the Young-Laplace equation [58]—$\Delta P = \gamma(1/R_1 + 1/R_2)$, where R_1 and R_2 are the radii of curvature in orthogonal planes. For a square cross-sectioned channel, we obtain $R_{\text{gutter}} = W/4$, and the deepest part of the gutter region will be

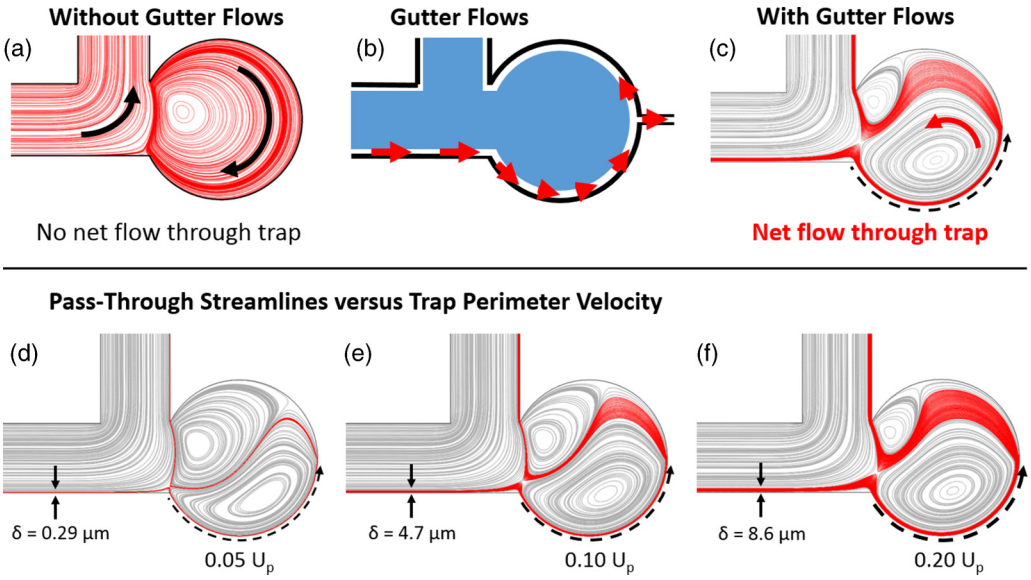

FIG. 4. Consequences of gutter-flow-induced advection on fluid circulation and mass transport. (a) Without gutter flows, fluid circulation is clockwise in the trap. Streamlines were obtained from a 2D COMSOL CFD simulation of single-phase Stokes flow past the open mouth of an enclosed circular trap. (b) Schematic illustrating how the outer-phase gutter flow will be distributed in the trap geometry. Red arrows indicate the outer-phase gutter flow along the perimeter of the aqueous phase (shaded blue). (c) In the presence of gutter flows, fluid circulation can be counterclockwise and also lead to enhanced mass transport due to streamlines that enter the trap and exit back into the plug. Streamline plots in (c)–(f) were generated from COMSOL CFD simulations where the bottom semicircular wall is moving at a fraction of the plug velocity, U_p, mimicking gutter flows. In red are highlighted the streamlines in a near-wall layer of thickness, δ, that pass through the trap region and exit into the bypass. In (c)–(f), the thickness of pass-through streamlines increases as the perimeter velocity around the trap increases.

$\approx W/10$, or 20 μm in our geometry. Thus, there could be significant flow within the gutter regions. The thin film regions, in contrast, likely have negligible flow, as film thickness for stationary droplets or droplets moving at extremely low Ca (Ca $< 10^{-5}$) is governed by the disjoining pressure and has been measured to be only 20–30 nm using reflection interface contrast microscopy [59].

The mechanism we propose for the counterclockwise circulation is that the continuous phase in the gutters flows along the perimeter of the plug and counterclockwise around the trapped droplet [as illustrated in Figs. 1(c) and 4(b)], countering the trap-entrance shear stresses—which would otherwise instigate clockwise circulation—and actually inducing circulation in the opposite direction. To incorporate the effect of gutter flows into our CFD simulation while still maintaining the simplicity of a single phase, we converted the lower half of the circular trap wall into a moving boundary [see Fig. 4(c)] with a prescribed velocity. A moving semicircular boundary mimics the effect of gutter flows, which would exert counterclockwise shear stress at the perimeter of the trap. The results are shown in Fig. 4(c), for the case where the boundary velocity is 20% of the mean plug velocity. We find that a set of streamlines that begin near the perimeter of the moving plug passes entirely through the trap region and exit back into the plug. This result is strikingly different from CFD simulations without gutter flows, as gutter flows appear to enable advection of material into and out of the trap region where previously there was no such exchange.

Based on our CFD simulations, we also note that the thickness, δ, of the set of pass-through streamlines increases with increasing perimeter velocities [see Figs. 4(d)–4(f)], suggesting mass transport out of the trap is enhanced by gutter-flow-induced advection (GFIA). For example, when

the perimeter velocity increases from 5% to 20% of the plug velocity, the thickness of the near-wall fluid layer with pass-through streamlines increases by 30-fold. It is also interesting to note that as the relative strength of the gutter flows—represented by the perimeter velocity—increases, the streamlines and locations of stagnation points all shift. This can be understood by realizing that the two counter-rotating vortices in the trap region correspond to the two opposing sources of shear stress: (1) a clockwise vortex in the upper left region induced by the flow within the plug passing by the entrance, and (2) a counterclockwise vortex in the lower right region induced by the gutter flows. As the balance of strength shifts between those opposing shear stresses, the size and location of the two corresponding vortices also shift.

More advanced versions of our model will therefore include the effects of GFIA, which stirs the fluid in the trapped droplets. To model GFIA, we implement the scheme shown in Fig. 2(c). A near-wall layer of fluid of predefined thickness δ from the moving plug is redirected into the trap region, follows the inner perimeter of the trap region, and then rejoins the moving plug. For ease of simulation and to reduce computation time, all particles within the trap-circulating path are moved with the same velocity—the "mean layer velocity," $\langle U_\delta \rangle$, which represents the average velocity of the fluid in the near-wall layer of the plug. This mean layer velocity is given by Eq. (4), which is obtained by integrating the velocity profile over the layer thickness and normalizing by that thickness.

$$\langle U_\delta \rangle = U_p \left[3\left(\frac{\delta}{W}\right) - 2\left(\frac{\delta}{W}\right)^2 \right]. \tag{4}$$

According to Eq. (4), if the layer thickness is 5% of the channel width ($\delta = 0.05\,W$), the mean layer velocity $\langle U_\delta \rangle$ is 14.5% of U_p. As δ increases, $\langle U_\delta \rangle$ increases, corresponding to increasing strength of GFIA relative to plug advection strength. In the simulations, we typically use $\delta/W < 0.125$.

When simulating GFIA, any particles within the near-wall layer that reach the trap interface region are redirected into the trap-circulating path. Particles are evenly distributed across the width of the trap-circulating path. Each time step, any particles in the trap-circulating path are advected according to the length of the time step and the mean layer velocity $\langle U_\delta \rangle$. Note, however, that particles are also allowed to diffuse in each time step. Particles may therefore diffuse into and out of the trap-circulating path. Once particles complete their journey around the perimeter of the trap, they are returned to the near-wall layer of the moving plug near the plug-trap interface.

IV. SIMULATION ALGORITHM

As described above, the most basic version of our phenomenological model [see Fig. 2(a)] considers advection and fluid recirculation within the plug and diffusion throughout the plug and any coalesced trapped droplets. To make it easier to implement the model in 2D particle-based simulations, the moving plug is approximated as a moving rectangle, and the traps with trapped droplets are approximated as squares. At the beginning of the simulation, all particles are contained within the enclosed traps, and the moving plug is void of particles. Once the moving plug has coalesced with a trapped droplet, the boundary between the trap and moving plug disappears, and particles are allowed to diffuse in and out of the trap. In each time step, particles within the plug are advected to their new locations, and particles are also allowed to diffuse. In simulations following more advanced versions of our model, the additional elements of CIA and/or GFIA are also addressed in each time step.

The following major steps are performed each time step in our simulations based on the phenomenological model (see Appendix B in ESI for more details):

(1) Allow coalescence and CIA between trap and moving plug if necessary.
(2) Allow diffusion of all particles using the random-walk method.
(3) Allow advection of fluid and particles, and execute GFIA if necessary.
(4) Update boundary locations for the moving plug—move all plug boundary segments forward at the mean plug velocity U_p.
(5) Check for plug detachment.
(6) Display and/or update graphical output if desired.

All the simulations were conducted using MATLAB (Release 2014a, The MathWorks, Inc.). The number of particles in each trap was typically 10 000 but was as high as 4×10^5 for visualization purposes. The time step size (Δt) in each simulation depends on the plug velocity and the length of the plug-trap interface (here, 200 μm) and is chosen so that the plug never moves more than the interface length in a single time step. Typically, the time steps are small enough so that multiple steps (e.g., anywhere from three to ten) are required for the plug to travel the length of the plug-trap interface. Time scales are nondimensionalized by the contact time (e.g., $t = t'/t_c$).

The implementation and impact of each major element of our phenomenological model (advection, diffusion, CIA, GFIA) depends on different sets of simulation parameters. For example, in the basic model, the control parameters are Pe and plug length (L_p). Likewise, CIA control parameters are L_i, L_x, W_{adv} and L_{adv}, and Δ_{merge}. The only control parameter for GFIA is the thickness of the near-wall layer of the plug (δ).

The values for control parameters used in simulation were obtained from our previous experimental studies [19,25] and are indicated in the relevant figure captions. In the simulations, the following parameters were directly obtained from experiments: U_p; L_p and plug volume (V_p); W and channel height (H); L_i; trap overhead area (which is converted into a square of the same area and of length, L_{trap}, for simulations), intertrap spacing (Δ_{trap}); and Δ_{merge}. Estimated simulation parameters included D, L_x, and δ.

In our Results and Discussion section, all length scales are normalized by the channel width, W' (e.g., L_p, L_x, δ)—except for L_x, which is normalized by the plug-trap interface length: $L_x = L'_x/L'_i$—and we denote dimensional lengths with a prime superscript (e.g., $L_p = L'_p/W'$), unless otherwise stated. Also note that in all simulations, the length of the plug-trap interface is equal to the width of the plug ($L_i = W$).

V. RESULTS AND DISCUSSION

First, in Sec. V A, we use our phenomenological model and present example results for the dilution of a single trap with a moving plug. In Sec. V B, we investigate how the microfluidic network geometry affects dilution and show that our simulation results can help explain some of the unique patterns observed in experimental concentration profiles. In Sec. V C, we study the importance of different mass transfer mechanisms on drop dilution by conducting a parametric study of the major model parameters, including the more advanced elements of CIA and GFIA. We compare their relative importance and show that GFIA can be extremely important. In Sec. V D, we argue that the overall dilution arising from different transport mechanisms can be understood in terms of two physical factors—duration and rate of mass transfer. Finally, in Sec. V E we show good quantitative agreement between our simulation predictions and experiment data of drop concentration profiles during dilution.

A. Mass transfer from a single trap—a representative simulation

Using the phenomenological model elements outlined in Sec. III and the simulation procedure discussed in Sec. IV, we simulated mass transfer during coalescence between a moving plug and a single trap. Figure 5 shows the sequence of images obtained from a representative simulation of a single aqueous trap preloaded with 400 000 dye particles being diluted with a pure water plug. The effects of all the transport mechanisms (advection within the plug, diffusion, delayed coalescence, CIA, and GFIA) have been included in the representative simulation (see also Video V1 in the Supplemental Material [60] and Appendix C in ESI).

In Fig. 5(a), the moving plug—completely devoid of particles—is approaching a trapped droplet with an initially uniform, high concentration of particles. In Fig. 5(b), the head of the plug moves some distance beyond the trapped droplet before coalescence, mimicking the delayed coalescence seen in experiments. Upon coalescence, there is coalescence-induced advection of particles, which causes some particles to be ejected upstream and downstream of the trap and also causes some of the lower-concentration plug fluid to infiltrate the trap.

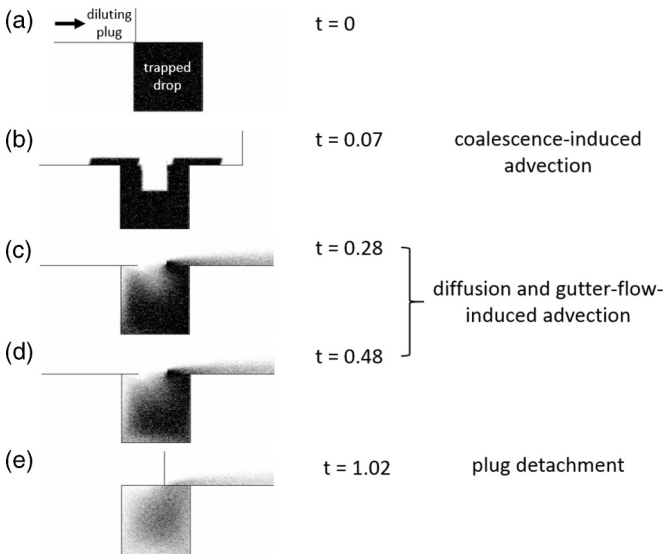

FIG. 5. Time-lapse images of the numerically simulated dilution of a single trap. The simulation was conducted at Pe = 160 with plug length of $L_p = 50$, and trap size of $L_{\text{trap}} = 2$. The parameters used for coalesced–induced advection are $L_i = 1$, $\Delta_{\text{merge}} = 2$, $L_x = 0.75$, $W_{\text{adv}} = 0.2$, and $L_{\text{adv}} = 1.41$. The parameters used for gutter-flow-induced advection are $\delta = 0.15$ (for which $U_d = 0.41U_p$).

As the coalesced moving plug continues to move downstream [Figs. 5(c) and 5(d)], gutter-flow-induced advection causes a gradual counterclockwise scooping of perimeter material out of the trap and into the plug. Simultaneously, there is diffusion of particles in all directions throughout the plug and trap. As particles exit the trap and into the plug (due to diffusion and GFIA), advection in the plug quickly carries those particles downstream. Notice how the width of the particle stream being carried away from the trap gradually increases in the downstream direction. This is evidence of diffusion across streamlines. Also we observe that the concentration—as indicated by the gray-scale darkness level—decreases over time, as seen from the time of coalescence [Fig. 5(b)] until the time of detachment [Fig. 5(e)]. Thus, our phenomenological modeling captures qualitatively the features seen in experiments.

B. Influence of microfluidic parking network geometry on drop dilution

We next considered whether our phenomenological model—first in its basic form with only plug advection, recirculation, and diffusion, and then in its full form including CIA and GFIA—could capture the effects of the MPN geometry. In MPNs such as the one shown in Fig. 1(a), there are two characteristics of the network geometry that periodically disturb what would otherwise be a consistent, repetitive pattern of trap-and-bypass loops [e.g., Fig. 1(b)]. First, from one row to the next, there is an alternation of the side with which traps coalesce with the moving plug. For example, relative to the head of the moving plug and facing downstream, the plug merges on the right side with the traps in the first row (bottom) but merges on the left side with traps in the second row. Second, note the additional length between rows, which could also affect dilution. In our model, these pattern-breaking characteristics can be included for additional realism and to study their effect on concentration profiles.

Figures 6(a)–6(c) are a set of images from our simulations showing the flexibility we have in testing different geometrical arrangements of the traps around the moving plug. In Fig. 6(a), the simplest arrangement is where all traps are evenly spaced apart and are on the same side of the plug. In Fig. 6(b), there are alternating groups of traps, but all traps are still evenly spaced apart. In

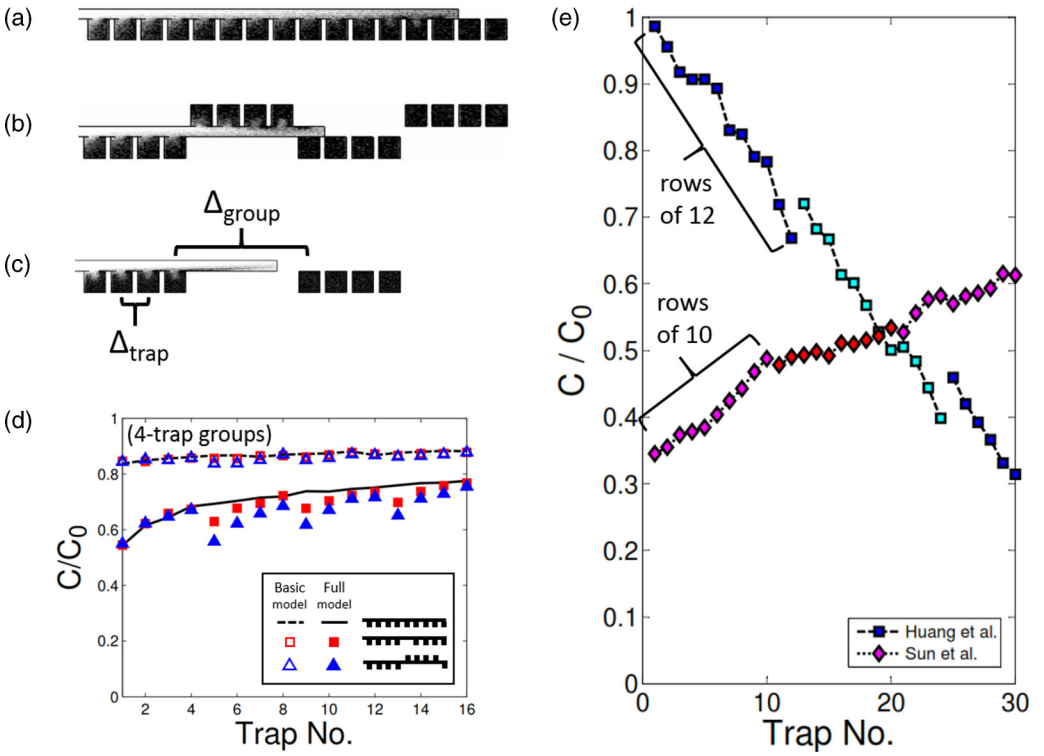

FIG. 6. Effect of microfluidic parking network geometry on droplet concentration profiles. Three network geometries were studied in the simulations using the both the basic and full phenomenological model: (a) All traps evenly spaced and on the same side of the plug; (b) alternating groups of traps; (c) multiple groups of traps on the same side of the plug but with larger distance between groups (Δ_{group}) than between traps (Δ_{trap}); (d) final droplet concentration profiles exhibit stairstepping segmentation when either there is additional space between groups of traps or when the side of coalescence shifts between groups; (e) final droplet concentration profiles for the first 30 traps in example dilution experiments by Huang *et al.* (trapped droplets diluting moving plug; Fig. 5(f) in Ref. [28]) and Sun *et al.* (moving plug diluting trapped droplets; 0.5 μl/m, 2.2-μl plug; Fig. 2(a) in Ref. [25]); alternating symbol-interior colors denote different rows of traps; stairstepping is seen between rows of traps. Simulation parameters are $L_p = 50, L_{\text{trap}} = 2, \Delta_{\text{trap}} = 2.5, \Delta_{\text{group}} = 10$, and Pe $= 160$.

Fig. 6(c), all traps are on the same side, but the distance between groups (Δ_{group}) is larger than the distance between traps (Δ_{trap}).

Figure 6(d) shows how the concentration profile changes when these MPN features are separately included in both the basic and full versions of our model. When the traps are all evenly spaced apart and are on the same side of the plug, the concentration gradations gradually increase. However, when there is additional space between groups of traps or when the side of coalescence shifts between groups, abrupt changes in the concentration profile are observed each time the network pattern shifts. In the particular set of simulations tested, these abrupt shifts—which look like stairstepping—are more strongly induced by changes in the side of coalescence than additional spacing between groups of traps, although this may change depending on the choice of parameters, such as intertrap spacing (Δ_{trap}) and diffusion coefficient (D).

The mechanism causing the abrupt decreases in concentration when the side of coalescence changes is due to the division of the moving plug into two circulating halves [see Fig. 2(a)]. As a result, dye particles that diffuse from traps into the plug on one side will tend to circulate only within that half, except for some diffusion across streamlines from one half to the other that occurs near the

center streamlines. This means that while the particle concentration increases on one side of the plug while it is coalesced with the first group of traps (e.g., on the right side of the plug), the concentration of the plug is still lower on the left side. Therefore when the plug finally coalesces with a group of traps on the other side (e.g., the left side of the plug), the lower concentration on the left side—and therefore greater concentration gradient—induces a greater degree of dilution of the first few traps on the left side than the previous few traps on the right side. The additional distance between groups of traps causes abrupt decreases in concentration for a similar reason: the additional distance gives particles more time to diffuse in all directions; therefore the previously high concentration near the walls that develops after a series of closely spaced traps has time to dissipate before reaching the next set of traps. This increases the concentration gradient between plug and trap for the next set of traps, thereby increasing the degree of dilution of the first few traps of the next group.

Comparing the results between the basic and full models in Fig. 6(d), we see that the inclusion of CIA and GFIA amplifies the abrupt shifts in concentration between rows or groups of traps. This is because the degree of stairstepping (abrupt shifts) depends on the balance of two opposing phenomena: (1) Mass transfer of solute from traps into the immediately adjacent side of the moving plug creates local disparities in concentration across the width of the plug, and (2) diffusion of solute tends to even out concentrations across the plug width. The faster the rate of mass transfer out of the traps is compared to the rate of diffusion, the more abrupt the stairstepping will be. Since CIA and GFIA both increase the overall mass transfer rate in and out of the traps, their inclusion in the model amplifies the stairstepping effect and decreases final concentrations, as seen in Fig. 6(d).

Experimental results [see Fig. 6(e)] reflect the same stairstepping segmentation of concentration profiles predicted by our simulations. In the experimental MPN shown in Fig. 1(a), there is additional channel length between each row (or group) of ten traps. As the moving plug reaches a new row, there is also a change in the side of coalescence. Both of these features contribute to the abrupt shifts in the concentration profiles [e.g., the Sun *et al.* profile in Fig. 6(e)] seen between the first few groups of ten traps. This stairstepping segmentation of concentration profiles is also evident from data reported by Huang *et al.* [28], but no mechanistic explanation was provided. Like the MPN in Fig. 1(a), the MPN used by Huang *et al.* had both a change in the side of coalescence and additional spacing between rows of traps. From the concentration profile of Huang *et al.* seen in Fig. 6(e) [and as shown in Fig. 5(f) of their study], stairstepping segmentation can be seen after the first two rows of 12 traps, supporting our explanation that the stairstepping of concentration profiles for certain SDAs is due to pattern-breaking geometric features. Thus, our phenomenological modeling highlights the important role that network geometry can play in coalescence-induced drop dilution.

Note that the concentration profile of Huang *et al.* [Fig. 6(e)] has a negative slope rather than a positive slope as seen in the concentration profiles of Sun *et al.* [Figs. 1(d), 1(e), and 6(e)]. This is because the moving plug in Huang *et al.* had a higher initial concentration of solute than the static droplets; therefore the net mass transfer was from the plug to the trapped droplets rather than from the trapped droplets to the plug. Because the concentration gradient is largest between the moving plug and the first trapped droplet, the greatest degree of mass transfer occurs in the first trap, and the first trap therefore attains a concentration closest to the initial concentration of the moving plug compared to the other traps. In Huang *et al.*, the first trap therefore had a high final concentration corresponding to an initially high concentration in the moving plug; in Sun *et al.*, the first trap had a low final concentration corresponding to an initially low concentration in the moving plug.

C. Importance of different mass transfer mechanisms on drop dilution

As discussed in Secs. V A and V B, simulations based on our phenomenological model can qualitatively explain many of the behaviors seen in experiments, such as advection of material exiting traps further downstream, diffusion across streamlines, CIA causing material to be advected both downstream and upstream of the trap, counterclockwise circulation within the trap, and abrupt shifts in concentration profiles. While having all model elements simultaneously present in simulations may result in more realistic behaviors, it is difficult to distinguish the impact of each element from

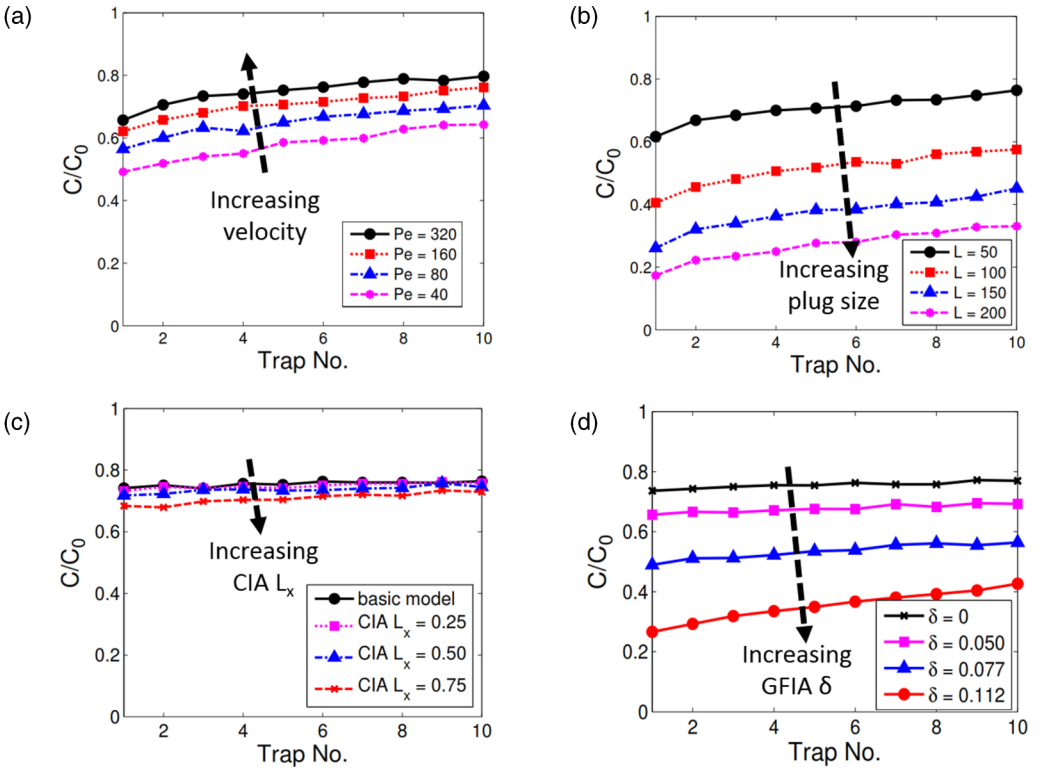

FIG. 7. Parametric studies on concentration profiles (final trap concentration normalized by initial concentration, C_o, versus trap number) in simulations. Unless otherwise stated, simulation parameters were $L_p = 100$; Pe $= 160$; $\delta = 0$; $L_x = 0$; $\Delta_{\text{trap}} = 5$ in (a), (b) and 10 in (c), (d); $W' = 200\mu$m; $L_{\text{trap}} = 2$; diffusion coefficient $D = 500\,\mu\text{m}^2/\text{s}$; 1×10^4 particles per trap. In (a), $L_p = 50$, and Pe was varied by varying plug velocity. In (b), normalized plug length was varied from $L_p = 50$ to 200. In (c), the trap-exchange area's normalized length (L_x) was varied from 0 to 0.75; $\Delta_{\text{merge}} = 3$. In (d), the solid colored lines denote a fixed Pe $= 166$ with GFIA δ varying from 0.050 to 0.112, and the dotted black line denotes no GFIA ($\delta = 0$) with Pe varying from 26 to 104 by altering diffusivity (D).

the others. Therefore we pursue a parametric investigation to gauge the relative importance of the identified transport mechanisms. To decouple the effects of pattern-breaking geometric features (as described in the previous section) from other possible phenomena, we simulate dilution using a plug moving past a simple linear array of ten traps, all on the same side of the plug and evenly spaced. We then investigate the importance of several major parameters—e.g., plug velocity, plug size, amount of CIA, relative strength of GFIA, and diffusion coefficient—by varying one parameter at a time while holding all others constant (see Fig. 7) and plotting the normalized concentration (C/C_0) versus trap number.

1. Basic model: Advection in plug plus diffusion

Using our basic model, which includes advection and recirculation within the moving plug and diffusion throughout all aqueous regions, we first investigate the dependence of final trap concentrations on parameters that can be controlled experimentally by altering the operating conditions: plug size (or length), and plug velocity. These two characteristics are adjusted in experiments simply by controlling the infusion and/or aspiration of the aqueous and oil phases, e.g., by starting or stopping syringe pumps and adjusting their volumetric flow rates. We first explore

the effect of plug velocity on dilution for a fixed plug length. Next, we explore the effect of plug length on dilution for a fixed plug velocity.

In Fig. 7(a), we observe that the final concentrations in each static droplet increase with increasing plug velocity (and increasing Pe), which is the same trend seen in experiments [Fig. 1(d)]. As plug velocity and Pe increase, there is less contact time between the moving plug and the trap. Because diffusion across streamlines is the only means for mass transfer in and out of the trap in the basic model, less contact time means less diffusion of particles out of the trap. Therefore as velocity increases, there is less dilution of the traps, and the final concentrations increase closer to their initial maximum values ($C/C_0 = 1$).

In Fig. 7(b), as plug size increases, final concentrations decrease. This corroborates the general trend seen in experiments [see Fig. 1(e)]. As plug size (characterized by plug length) increases for a fixed plug velocity, there is greater contact time and therefore more time for material to diffuse out from the traps. As a result, concentrations decrease with increasing plug length.

2. Basic model with coalescence-induced advection

We now investigate the influence of CIA by adding it to our basic model. As explained in Sec. III C and illustrated in Fig. 2(c), CIA is simulated by swapping the fluid contents of predefined trap-exchange and plug-exchange areas. Because the degree of volume exchange (or area exchange in 2D) is likely dictated by the size of the plug-trap interface (L_i), we approximate the trap-exchange area as a square region with $L_x \leqslant L_i$. To gauge the effect of CIA, we simulate a moving plug coalescing with a trapped droplet after a fixed amount of overshoot (i.e., delayed coalescence; $\Delta_{\text{merge}} = 3$), and we vary the size of the trap-exchange area (which then dictates the size of the plug-exchange areas) up to its maximum dimensions. Plug length and plug velocity (and therefore also Pe) are kept constant. After coalescence, the basic model elements of advection and recirculation in the plug and diffusion throughout the aqueous regions are employed until detachment.

Figure 7(c) shows final concentration profiles for several different amounts of CIA (by varying L_x). As the trap-exchange area increases, final concentrations decrease due to an increase in the amount of dye material that is initially advected out of the trap upon coalescence. Note, however, that for long diluting plugs as discussed herein (as opposed to short droplets), the effect of CIA on concentration is minimal compared to the other parameters. Even when the trap-exchange area is 75% of its theoretical maximum value ($L_x = 0.75$), CIA decreases final concentrations by only 6% in the first trap and even less in later traps. The effect of CIA on dilution is therefore minimal when using long plugs.

3. Basic model with gutter-flow-induced advection

Next we assess the importance of GFIA on dilution by adding it to our basic model. As described in Sec. III D, the relative strength of GFIA in our simulations is dictated by δ, which defines the thickness of the trap-perimeter region with pass-through streamlines. Holding plug length and plug velocity (and therefore Pe) constant, we varied δ and examined the resulting concentration profiles after dilution.

Figure 7(d) includes concentration profiles for three values of GFIA δ. As the relative strength of GFIA is increased (by increasing δ), the total amount of mass transfer between the trap and plug increases, yielding lower final concentrations. Increasing δ [see Fig. 2(d)] effectively enlarges the fraction of the trap affected by pass-through streamlines, which enables a greater amount of scooping of perimeter material out of the trap and therefore greater rate and degree of mass transfer. Thus, the mass transfer rate in and out of the trap increases as GFIA δ increases, leading to faster dilution and lower final trap concentrations.

Based on the parametric studies shown in Fig. 7 where we independently varied plug velocity, plug length, CIA, and GFIA, we can compare the relative importance of each parameter on mass transfer. From our analysis of Pe and contact time in Sec. II A, we would naturally expect both plug velocity and plug length to be important. Indeed, we do find that both parameters can strongly

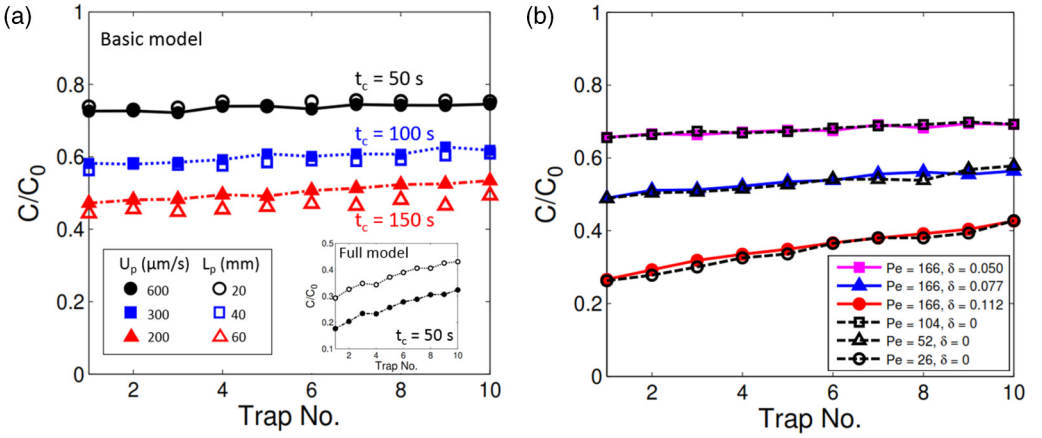

FIG. 8. Contact time and mass transfer rate dictate final concentrations for basic model: (a) Simulations using basic model with the same contact time yield virtually the same results so long as the ratio of plug length (L_p) and plug velocity (U_p) remains constant; solid symbols denote varying plug velocity with constant plug length, $L_p = 30$ mm; open symbols denote varying plug length with constant plug velocity, $U_p = 400\,\mu$m/s; inset shows mismatch for same contact time, $t_c = 50$ s, when using the full model, which includes CIA ($L_x = 0.75$, $W_{\text{adv}} = 0.2$, and $L_{\text{adv}} = 1.41$) and GFIA ($\delta = 0.1$); (b) simulations with the same set of mass transfer rates in and out of each trap yield virtually the same results regardless of the precise values of the controlling parameters, GFIA δ and D. Unless otherwise stated, simulation parameters in (b) were $L_p = 100$; Pe $= 160$; $\delta = 0$; $L_x = 0$; $\Delta_{\text{trap}} = 10$; $W' = 200\,\mu$m; $L_{\text{trap}} = 2$; diffusion coefficient $D = 500\,\mu\text{m}^2/\text{s}$; 1×10^4 particles per trap. Solid colored lines in (b) denote a fixed Pe $= 166$ with GFIA δ varying from 0.050 to 0.112, and the dotted black line denotes no GFIA ($\delta = 0$) with Pe varying from 26 to 104 by altering diffusivity.

affect dilution. Regarding the size of the CIA trap-exchange area and GFIA δ, both of which were based on unexpected experimental observations, we found that while the effect of CIA was relatively insignificant, GFIA had a significant impact on dilution. Thus, plug velocity, plug length, and GFIA δ should all be considered when trying to estimate final concentrations.

D. Duration and rate of mass transfer dictate drop dilution

The results in Sec. V C indicate that the transport mechanisms dominating the dilution process are diffusion, Hagen-Poiseuille-like recirculation in the moving plug, and GFIA. In particular, we found that parameters such as plug velocity, plug length, and GFIA δ play an important role in dictating the final concentrations in the trapped drops. In this section, we present a conceptual framework that synthesizes the influence of these different transport mechanisms and their governing parameters into two physical factors that control the overall dilution process. First is the duration of mass transfer, which is regulated by the contact time between the moving plug and the stationary drops. Second is the rate of mass transfer which depends on both the diffusion coefficient and the magnitude of δ that controls the strength of GFIA. Below we present results that support this conceptual framework.

The duration of mass transfer depends on the contact time, $t_c = L_p/U_p$, which is the ratio of plug length to plug velocity. Thus, any two combinations of plug length and plug velocity with the same ratio should yield the same result—assuming a constant mass transfer rate. To test this, we use the basic model where diffusivity is the only mass transfer rate parameter. Figure 8(a) confirms our hypothesis. It shows how different combinations of plug velocity and plug length that share the same contact times yield virtually the same final trap concentrations. Note that here we have used the basic model, rather than the full model, since in the full model, changing plug velocity also changes the mass transfer rate through GFIA and CIA. As a result, in the full model, two different pairs of

plug velocity and plug length with the same contact time no longer yield the same dilution results [see inset of Fig. 8(a)].

We note that although contact time appears to scale out the effects of plug velocity and length, in Fig. 8(a), we observe that the longest contact time ($t_c = 150\,\mathrm{s}$) evidenced some disagreement between two sets of plug velocity and plug length. This is because one of the simulations was conducted at a lower Pe = 80 (the open triangle symbols with $U_p = 200\,\mu\mathrm{m/s}$) and the other was conducted at a higher Pe = 160 (the solid triangle symbols with $U_p = 400\,\mu\mathrm{m/s}$). When Pe is high, any solute particles that diffuse out of the trap are quickly cleared downstream and away from the trap entrance, meaning that the trap's exiting particles do not greatly affect the local plug-trap concentration gradient; thus only diffusion time (i.e., contact time) matters. When Pe is low, however, changes in plug velocity can more noticeably affect the concentration gradient near the trap entrance. Since concentration gradient affects mass transfer rate, and velocity changes at low Pe will alter concentration gradients, contact time will be a less effective predictor of dilution for low Pe.

Next, we considered the impact of rate of mass transfer on drop dilution. Both GFIA and diffusion affect the rate of mass transfer. We therefore hypothesized that by varying diffusivity, it should be possible to affect the dilution and final concentration profiles in the same manner as varying the relative strength of GFIA. To test this hypothesis, we first simulated the dilution of ten traps with a moving plug of fixed length and fixed velocity for three different values of diffusivity (and therefore Pe) and no GFIA [see Fig. 8(b)]. Then we conducted another three simulations, but this time we held the diffusivity (and therefore Pe) constant while testing three different values of GFIA δ. The values for δ were chosen such that the first-trap concentrations matched those obtained when investigating different values of diffusivity and Pe.

Quite remarkably, the three curves for the Pe investigation almost perfectly matched the three curves for the GFIA investigation. For example, the concentrations obtained when Pe = 166 and $\delta = 0.050$ nearly exactly match those when Pe = 104 and $\delta = 0$ (no GFIA). This good agreement indicates that the final concentration profiles depend only on overall rates of mass transfer in and out of the traps and the overall time for mass transfer (contact time)—i.e., total amount of mass transfer—regardless of the exact mechanism of mass transfer.

E. Comparison between experimental and simulation results

We wanted to evaluate how closely our full-model simulations could predict the dilution profiles for the first ten traps (i.e., the first row) of the SDA shown in Fig. 1(a). In our simulations, we selected parameter values to reflect the experimentally observable conditions, including W, $L_{\mathrm{trap}}, L_p, U_p, L_x, W_{\mathrm{adv}}, L_{\mathrm{adv}}$, and D. Because GFIA δ was the only unknown simulation parameter, our approach to setting this simulation parameter for each volumetric flow rate (and corresponding U_p) was to first repeatedly simulate the dilution of only the first trapped droplet for varying values of δ until the final concentration was close to experimental observations (e.g., error of $\leqslant 4\%$ of initial trap concentration). After identifying reasonable values of δ for each flow rate (and U_p) from the first-trap simulation, we then asked whether these best-fit δ values would successfully predict the dilution profile of the remaining nine consecutive and evenly spaced traps.

Figure 9 is a comparison of final concentration profiles for experiments [25] and simulations at different volumetric flow rates using the δ values that were determined as previously mentioned. As seen in Fig. 9, the simulations generally offer a good quantitative match with experiments. However, there is noticeable deviation in at least the last few traps in each case. Thus, while our full model is able to reasonably predict the dilution of the first few traps, it would likely yield large errors for larger systems, such as the entire 60-trap SDA in Fig. 1(a). One possible explanation for this is that we have considered a simplified description of the microfluidic network and ignored other geometric details such as the effects of bends and circular trap shape.

An interesting outcome of our efforts to match simulations with experiments is that we find a nonlinear power-law dependence between the GFIA δ and U_p: GFIA $\delta = (516 \pm 63) U_p^{-0.70\pm0.03}$. We observed that the relative strength of GFIA must decrease with increasing plug velocity in order for

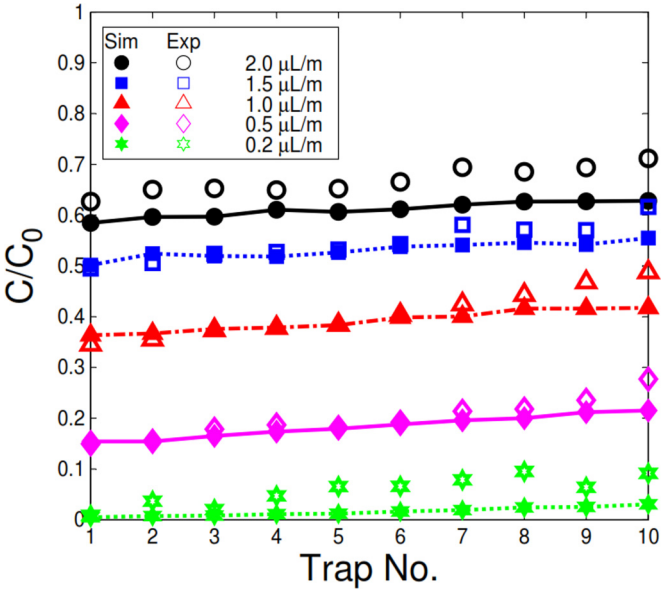

FIG. 9. Comparison of final concentration profiles for simulations and experiments at different volumetric flow rates. Experimental data from Sun *et al.*, Fig. 2(a) in Ref. [25] [also shown in Fig. 1(d) in log-lin scale]; 2.2-μl plug (55 mm long), 450-μm-diameter traps. Simulations based on full model (including CIA and GFIA) with the following parameters: $L_p = 275$ (55 mm); $L_{\text{trap}} = 2$ (equivalent area to 450-μm-diameter circular trap); $U_p = 83$–$832\,\mu$m/s, corresponding to 0.2–2.0 μl/m for 200-μm-tall channels; $D = 500\,\mu\text{m}^2/\text{s}$; $L_x = 0.75$; $W_{\text{adv}} = 0.2$; $L_{\text{adv}} = 1.41$.

the data to match in Fig. 9. This dependence explains how it is possible for an order-of-magnitude change in velocity (by changing volumetric flow rate from 0.2 to 2.0 μl/m) to yield nearly two orders-of-magnitude change in final concentration, evident in Fig. 1(d). Hypothetically, if the mass transfer in and out of the trap were solely due to diffusion, then the rate of mass transfer should be roughly constant, and contact time would dictate the degree of dilution. An order-of-magnitude increase in contact time (by decreasing volumetric flow rate from 2.0 to 0.2 μl/m) should therefore yield less than one order-of-magnitude change in final concentration, as diffusion distance depends on the square root of time [see Eq. (2)]. However, the nonlinear dependence of GFIA δ on plug velocity suggests that the mass transfer rate is in fact not constant and in reality increases with decreasing velocity. This makes it possible for an order-of-magnitude change in velocity to yield a nearly two orders-of-magnitude change in dilution.

The physical significance of this nonlinear, inverse relationship between GFIA δ and U_p is that the relative strength of GFIA appears to decrease as plug velocity increases. Since GFIA is driven by gutter flows, this relationship implies that gutter flows—compared to main channel flows—weaken with increasing plug velocity. This is likely due to the trapped droplet increasingly deforming against the trap-exit constriction as plug velocity and pressure differential across the trap increase, which would decrease the available cross-sectional area for gutter flows (i.e., decrease the gutter size). Measurement of the "leaky" flow rate around the trapped drop as a function of main-channel Ca by Bithi *et al.* [26] [in an SDA as shown in Fig. 1(a)] supports this argument. In that study, as Ca increases, the leaky flow rate around a trapped droplet decreases and quickly becomes negligible after a critical Ca due to the deformed drop pressing against the trap constriction. Further experiments will be required to determine whether the gutter size, gutter velocity, and the relative strength of GFIA do indeed decrease with increasing plug velocity.

VI. CONCLUSIONS

Because of the increasing use of microfluidic static droplet arrays (SDAs) in producing arrays of trapped droplets with gradients in concentration, there is a need for a deeper understanding of the physical phenomena that dictate mass transfer in such networks. We therefore developed a simple phenomenological model for the dilution of SDAs with moving plugs. Our model has enabled us to identify the key phenomena that dictate mass transfer in these systems, which can help in designing better devices to predictably control the dilution of droplet arrays. The key phenomena include (1) advection within the moving plug, (2) diffusion throughout all aqueous regions, (3) coalescence-induced advection (CIA), and (4) gutter-flow-induced advection (GFIA).

Our basic phenomenological model considers only advection within the moving plug and diffusion throughout the plug and any coalesced droplets. Simulations based on this simple model yielded the same qualitative trends seen in experiments of long moving plugs diluting SDAs: increasing plug length and decreasing plug velocity both decrease final concentrations. Furthermore, despite the simplicity of our basic model we were able to verify that the staircase segmentation of the SDA concentration profiles observed in experiments is due to (1) periodic alternation of the side of coalescence between the moving plug and the static droplets, and (2) additional channel length between rows of static droplets.

A parametric study of the key mass transfer phenomena enabled us to gauge the relative importance of each phenomenon. As expected, plug velocity and plug length are both important to the degree of dilution. While CIA does slightly decrease final concentrations, its effect is minimal compared to GFIA. Approximating GFIA simply by redirecting a fraction of the plug's advective flow through the trap along its perimeter, we were able to demonstrate the significant impact that gutter flows can have on dilution rate and final trap concentrations.

With a multitude of model parameters that can affect mass transfer, we searched for an underlying physics-based framework that could better explain how each of these parameters relate to one another and affect dilution. We find that all parameters can be divided into two main drivers for dilution: (1) those affecting the duration of mass transfer—i.e., contact time (e.g., plug velocity and plug length), and (2) those affecting the rate of mass transfer (e.g., GFIA, CIA, diffusivity). Particular attention should be paid to GFIA, as its importance may have been previously underestimated or even overlooked.

Our identification of GFIA as an alternative transport mechanism that depends nonlinearly on plug velocity has significant implications. With respect to the dilution of SDAs, the presence or absence of GFIA can impact the design and operation of microfluidic devices. Alternatively, gutter-flow-induced mass transfer can lead to efficient methods of oil recovery from droplets trapped in porous media.

ACKNOWLEDGMENT

This work was supported by the National Science Foundation (CAREER Award No. CBET: 1150836).

[1] L. Li and R. F. Ismagilov, Protein crystallization using microfluidic technologies based on valves, droplets, and SlipChip, Biophysics **39**, 139 (2010).

[2] D. G. Anderson, S. Levenberg, and R. Langer, Nanoliter-scale synthesis of arrayed biomaterials and application to human embryonic stem cells, Nat. Biotechnol. **22**, 863 (2004).

[3] E. Brouzes, M. Medkova, N. Savenelli, D. Marran, M. Twardowski, J. B. Hutchison, J. M. Rothberg, D. R. Link, N. Perrimon, and M. L. Samuels, Droplet microfluidic technology for single-cell high-throughput screening, Proc. Natl. Acad. Sci. USA **106**, 14195 (2009).

[4] J. J. Agresti, E. Antipov, A. R. Abate, K. Ahn, A. C. Rowat, J.-C. Baret, M. Marquez, A. M. Klibanov, A. D. Griffiths, and D. A. Weitz, Ultrahigh-throughput screening in drop-based microfluidics for directed evolution, Proc. Natl. Acad. Sci. USA **107**, 4004 (2010).

[5] M. T. Guo, A. Rotem, J. A. Heyman, and D. A. Weitz, Droplet microfluidics for high-throughput biological assays, Lab Chip **12**, 2146 (2012).
[6] C. N. Baroud, F. Gallaire, and R. Dangla, Dynamics of microfluidic droplets, Lab Chip **10**, 2032 (2010).
[7] G. F. Christopher and S. L. Anna, Microfluidic methods for generating continuous droplet streams, J. Phys. D **40**, R319 (2007).
[8] M. Prakash and N. Gershenfeld, Microfluidic bubble logic, Science **315**, 832 (2007).
[9] S. L. Anna, Droplets and bubbles in microfluidic devices, Annu. Rev. Fluid Mech. **48**, 285 (2016).
[10] B. Zheng, J. D. Tice, L. S. Roach, and R. F. Ismagilov, A droplet-based, composite PDMS/glass capillary microfluidic system for evaluating protein crystallization conditions by microbatch and vapor-diffusion methods with on-chip x-ray diffraction, Angew. Chem., Int. Ed. **43**(19), 2508 (2004).
[11] O. J. Miller, A. El Harrak, T. Mangeat, J.-C. Baret, L. Frenz, B. El Debs, E. Mayot, M. L. Samuels, E. K. Rooney, P. Dieu, M. Galvan, D. R. Link, and A. D. Griffiths, High-resolution dose–response screening using droplet-based microfluidics, Proc. Natl. Acad. Sci. USA **109**, 378 (2012).
[12] M. Sun and Q. Fang, High-throughput sample introduction for droplet-based screening with an on-chip integrated sampling probe and slotted-vial array, Lab Chip **10**, 2864 (2010).
[13] H. Song and R. F. Ismagilov, Millisecond kinetics on a microfluidic chip using nanoliters of reagents, J. Am. Chem. Soc. **125**, 14613 (2003).
[14] L.-F. Cai, Y. Zhu, G.-S. Du, and Q. Fang, Droplet-based microfluidic flow injection system with large-scale concentration gradient by a single nanoliter-scale injection for enzyme inhibition assay, Anal. Chem. **84**, 446 (2011).
[15] A. B. Theberge, G. Whyte, and W. T. Huck, Generation of picoliter droplets with defined contents and concentration gradients from the separation of chemical mixtures, Anal. Chem. **82**, 3449 (2010).
[16] M.-P. N. Bui, C. A. Li, K. N. Han, J. Choo, E. K. Lee, and G. H. Seong, Enzyme kinetic measurements using a droplet-based microfluidic system with a concentration gradient, Anal. Chem. **83**, 1603 (2011).
[17] R. M. Lorenz, G. S. Fiorini, G. D. Jeffries, D. S. Lim, M. He, and D. T. Chiu, Simultaneous generation of multiple aqueous droplets in a microfluidic device, Anal. Chim. Acta **630**, 124 (2008).
[18] N. Damean, L. F. Olguin, F. Hollfelder, C. Abell, and W. T. Huck, Simultaneous measurement of reactions in microdroplets filled by concentration gradients, Lab Chip **9**, 1707 (2009).
[19] M. Sun and S. A. Vanapalli, Generation of chemical concentration gradients in mobile droplet arrays via fragmentation of long immiscible diluting plugs, Anal. Chem. **85**, 2044 (2013).
[20] X. Niu, F. Gielen, J. B. Edel, and A. J. deMello, A microdroplet dilutor for high-throughput screening, Nat Chem. **3**, 437 (2011).
[21] P. M. Korczyk, L. Derzsi, S. Jakieła, and P. Garstecki, Microfluidic traps for hard-wired operations on droplets, Lab Chip **13**, 4096 (2013).
[22] A. R. Abate, T. Hung, P. Mary, J. J. Agresti, and D. A. Weitz, High-throughput injection with microfluidics using picoinjectors, Proc. Natl. Acad. Sci. USA **107**, 19163 (2010).
[23] B. Bhattacharjee and S. A. Vanapalli, Electrocoalescence based serial dilution of microfluidic droplets, Biomicrofluidics **8**, 044111 (2014).
[24] E. Fradet, C. Mcdougall, P. Abbyad, R. Dangla, D. Mcgloin, and C. N. Baroud, Combining rails and anchors with laser forcing for selective manipulation within 2D droplet arrays, Lab Chip **11**, 4228 (2011).
[25] M. Sun, S. S. Bithi, and S. A. Vanapalli, Microfluidic static droplet arrays with tuneable gradients in material composition, Lab Chip **11**, 3949 (2011).
[26] S. S. Bithi, W. S. Wang, M. Sun, J. Blawzdziewicz, and S. A. Vanapalli, Coalescing drops in microfluidic parking networks: A multifunctional platform for drop-based microfluidics, Biomicrofluidics **8**, 034118 (2014).
[27] H. Wen, Y. Yu, G. Zhu, L. Jiang, and J. Qin, A droplet microchip with substance exchange capability for the developmental study of C. elegans, Lab Chip **15**, 1905 (2015).
[28] X. Huang, W. Hui, C. Hao, W. Yue, M. Yang, Y. Cui, and Z. Wang, On-site formation of emulsions by controlled air plugs, Small **10**, 758 (2014).
[29] J. Shemesh, T. B. Arye, J. Avesar, J. H. Kang, A. Fine, M. Super, A. Meller, D. E. Ingber, and S. Levenberg, Stationary nanoliter droplet array with a substrate of choice for single adherent/nonadherent cell incubation and analysis, Proc. Natl. Acad. Sci. USA **111**, 11293 (2014).

[30] A. Anilkumar, C. Lee, and T. Wang, Surface-tension-induced mixing following coalescence of initially stationary drops, Phys. Fluids A **3**, 2587 (1991).
[31] F. Blanchette, Simulation of Mixing within Drops Due to Surface Tension Variations, Phys. Rev. Lett. **105**, 074501 (2010).
[32] Y. Zhang, S. D. Oberdick, E. R. Swanson, S. L. Anna, and S. Garoff, Gravity driven current during the coalescence of two sessile drops, Phys. Fluids (1994-present) **27**, 022101 (2015).
[33] D. Chen, R. Cardinaels, and P. Moldenaers, Effect of confinement on droplet coalescence in shear flow, Langmuir **25**, 12885 (2009).
[34] V. van Steijn, C. R. Kleijn, and M. T. Kreutzer, Flows around Confined Bubbles and Their Importance in Triggering Pinch-Off, Phys. Rev. Lett. **103**, 214501 (2009).
[35] V. van Steijn, M. T. Kreutzer, and C. R. Kleijn, μ-PIV study of the formation of segmented flow in microfluidic T-junctions, Chem. Eng. Sci. **62**, 7505 (2007).
[36] J. J. Hawkes, R. W. Barber, D. R. Emerson, and W. T. Coakley, Continuous cell washing and mixing driven by an ultrasound standing wave within a microfluidic channel, Lab Chip **4**, 446 (2004).
[37] T. Casalini, M. Salvalaglio, G. Perale, M. Masi, and C. Cavallotti, Diffusion and aggregation of sodium fluorescein in aqueous solutions, J. Phys. Chem. B **115**, 12896 (2011).
[38] H. Wong, C. Radke, and S. Morris, The motion of long bubbles in polygonal capillaries. Part 2. Drag, fluid pressure and fluid flow, J. Fluid Mech. **292**, 95 (1995).
[39] K. Handique and M. A. Burns, Mathematical modeling of drop mixing in a slit-type microchannel, J. Micromech. Microeng. **11**, 548 (2001).
[40] Z. Che, T. N. Wong, and N.-T. Nguyen, An analytical model for a liquid plug moving in curved microchannels, Int. J. Heat Mass Transfer **53**, 1977 (2010).
[41] Z. Che, T. N. Wong, and N.-T. Nguyen, An analytical model for plug flow in microcapillaries with circular cross section, Int. J. Heat Fluid Flow **32**, 1005 (2011).
[42] Z. Che, N.-T. Nguyen, and T. N. Wong, Analysis of chaotic mixing in plugs moving in meandering microchannels, Phys. Rev. E **84**, 066309 (2011).
[43] M. N. Kashid, I. Gerlach, S. Goetz, J. Franzke, J. Acker, F. Platte, D. Agar, and S. Turek, Internal circulation within the liquid slugs of a liquid-liquid slug-flow capillary microreactor, Ind. Eng. Chem. Res. **44**, 5003 (2005).
[44] H. C. Berg, *Random Walks in Biology* (Princeton University Press, Princeton, NJ, 1993).
[45] R. Phillips, J. Kondev, J. Theriot, and H. Garcia, *Physical Biology of the Cell* (Garland Science, New York, 2012).
[46] P. C. Bressloff, *Stochastic Processes in Cell Biology* (Springer, Berlin, 2014), Vol. 41.
[47] T. S. Ursell, The diffusion equation: a multi-dimensional tutorial, California Institute of Technology, Pasadena, Technical Report, 2007.
[48] D. P. Ziegler, Boundary conditions for lattice Boltzmann simulations, J. Stat. Phys. **71**, 1171 (1993).
[49] S. Chen and G. D. Doolen, Lattice Boltzmann method for fluid flows, Annu. Rev. Fluid Mech. **30**, 329 (1998).
[50] P. T. Jaeger, J. Janssen, F. Groeneweg, and W. Agterof, Coalescence in emulsions containing inviscid drops with high interfacial mobility, Colloids Surf., A **85**, 255 (1994).
[51] R. Kirkpatrick and M. Lockett, The influence of approach velocity on bubble coalescence, Chem. Eng. Sci. **29**, 2363 (1974).
[52] P. De Bruyn, R. Cardinaels, and P. Moldenaers, The effect of geometrical confinement on coalescence efficiency of droplet pairs in shear flow, J. Colloid Interface Sci. **409**, 183 (2013).
[53] A. S. Basu and Y. B. Gianchandani, Virtual microfluidic traps, filters, channels and pumps using Marangoni flows, J. Micromech. Microeng. **18**, 115031 (2008).
[54] S. Bianchini, A. Lage, T. Siu, T. Shinbrot, and E. Altshuler, Upstream contamination by floating particles, Proc. R. Soc. A **469**, 20130067 (2013).
[55] J. F. Hernández-Sánchez, A. Eddi, and J. Snoeijer, Marangoni spreading due to a localized alcohol supply on a thin water film, Phys. Fluids (1994-present) **27**, 032003 (2015).
[56] C. Giles and A. Soutar, Surface tension of ionised dye solutions, J. Soc. Dyers Colour. **87**, 301 (1971).

[57] K. Chang, G. Constantinescu, and S.-O. Park, Analysis of the flow and mass transfer processes for the incompressible flow past an open cavity with a laminar and a fully turbulent incoming boundary layer, J. Fluid Mech. **561**, 113 (2006).

[58] W. M. Deen, *Analysis of Transport Phenomena, Topics in Chemical Engineering* (Oxford University Press, New York, 1998), Vol. 3.

[59] A. Huerre, O. Theodoly, A. M. Leshansky, M.-P. Valignat, I. Cantat, and M.-C. Jullien, Droplets in Microchannels: Dynamical Properties of the Lubrication Film, Phys. Rev. Lett. **115**, 064501 (2015).

[60] See Supplemental Material at http://link.aps.org/supplemental/10.1103/PhysRevFluids.xx.xxxxxx for implementation of recirculating flow in simulations, simulation algorithm, and an example simulation video.